

SCIENTIFIC REPORTS

OPEN

Interaction of Glide Dislocations with Extended Precipitates in Mg-Nd alloys

Zhihua Huang, John E. Allison & Amit Misra

The unit processes of precipitate-dislocation interaction in dilute Mg-Nd alloys are elucidated through *in situ* indentation experiments in TEM. Results suggest that pinned dislocations can glide along the broad facets of extended β_1 precipitates, a common strengthening phase in Mg-rare earth (RE) alloys. A dislocation-theory based analysis suggests that the shape, spacing and orientation (with respect to the glide plane) of β_1 precipitates may favor glide of pinned dislocations along interfaces as opposed to the classical mechanism of bowing and looping around the precipitate.

As the lightest structural metal, magnesium is becoming increasingly important for light weighting strategies as fuel efficiency is of great concern to industries such as automotive^{1,2} and aerospace³. For many magnesium alloys, precipitation hardening is an important mechanism for impeding dislocations on the basal glide planes. In particular, precipitates that are aligned parallel to the prism planes, so-called prismatic precipitates, have been shown to be effective in pinning basal dislocations^{4,5}. Commercial alloys such as WE54, WE43 and Mg-RE (RE represents rare earth element) utilize the prismatic β_1 precipitate as a strengthening phase⁶⁻⁸. The β_1 phase has an ordered structure DO_3 (space group $Fm\bar{3}m$, $a_{\beta_1} = 0.74$ nm) with a composition of Mg_3RE^9 , and is generally regarded as non-shearable by basal slip in Mg matrix¹⁰.

For non-shearable precipitates, the increase in critical resolved shear stress (CRSS), τ_{Orowan} , may be estimated by the Orowan mechanism of dislocation bowing and looping around an array of point obstacles¹¹⁻¹⁴. The equation is given as

$$\tau_{Orowan} = \frac{Gb}{2\pi\lambda\sqrt{1-\nu}} \ln \frac{d_p}{r_0} \quad (1)$$

where λ is the inter-particle spacing in the slip plane, d_p and r_0 are outer and inner cut-off radii for calculation of dislocation energy, G is shear modulus of the matrix phase, b is the magnitude of the Burgers vector, and ν is Poisson's ratio. However, in practical alloys such as Mg-RE alloys, precipitates may have finite sizes and a non-spherical or non-equiaxed shape. Certain corrections have been made to include precipitate shape and orientation effects in equation (1). Stark *et al.*¹⁵ worked on the self-stress effect of dislocation caused by different precipitate-dislocation configurations. Nie *et al.*⁵ on the other hand, studied the effect of precipitate distribution and morphology on inter-particle spacing. Several attempts to simulate dislocation-precipitate interaction have also been made by dislocation dynamics (DD) and phase-field^{16,17} in which the essence of interaction is still based on Orowan strengthening. Although there are many attempts to correct or simulate the Orowan mechanism, the dynamic processes for dislocations overcoming the precipitates remain unclear. Direct visualization of dislocation-precipitate interactions will be critical in developing physics-based models of unit mechanisms that can also be inputs for dislocation dynamics simulation¹⁸ with predictive capability.

In the present work, *in situ* indentation in the TEM has been used to study the unit processes of precipitate-dislocation interaction in a dilute Mg-Nd alloy. The observed interactions are rationalized using a dislocation-theory based analysis.

Results

Two scenarios are presented in this section viewing the precipitate-dislocation interactions from either $\langle 0001 \rangle$ or $\langle \bar{1}2\bar{1}3 \rangle$ orientations. The β_1 precipitates have a lath morphology and are parallel to the $(10\bar{1}0)$ habit plane. The orientation relationship between β_1 precipitates and matrix is $[10\bar{1}0]_m \parallel [\bar{1}12]_p$ and $(0001)_m \parallel (110)_p$. The precipi-

Department of Materials Science and Engineering, University of Michigan, Ann Arbor, United States. Correspondence and requests for materials should be addressed to Z.H. (email: huzhuhua@umich.edu)

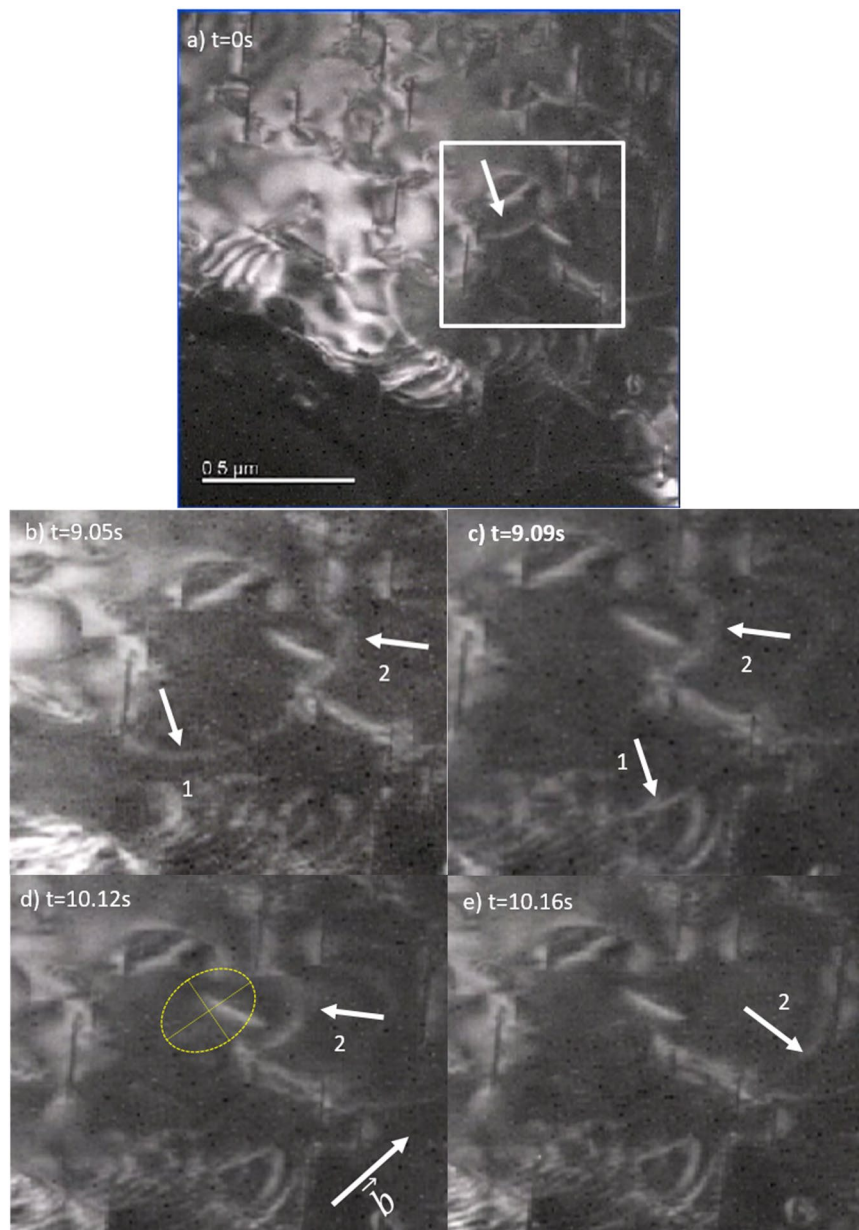


Figure 1. TEM images of dislocation glide on the basal plane. The region in Fig. 1b,c,d,e are from the marked region in Fig. 1a. The time interval between (b) and (c), (d) and (e) is very short (one frame 0.04 s) recording the dislocation propagation for both segments. Frame (d) shows an elliptical shape of the bowed dislocation segment 2.

tates have a high aspect ratio and are approximately 200 nm along both length $[\bar{1}2\bar{1}0]$ and height $[0001]$ dimensions but only 10 nm in thickness. In the over-aged aging condition studied (9 hours at 250 °C), the β_1 precipitates are prone to be semi-coherent. In order to have the best contrast, both bright field and dark field diffraction conditions were used. For the (0001) view plane, dark field imaging was used and dislocations appear as bright lines in section 2.a (Supplementary video 2.a) whereas for the $(\bar{1}2\bar{1}3)$ view plane, bright field imaging was used and dislocations appear as dark lines in section 2.b (Supplementary video 2.b). The *in situ* experiments were supplemented with post mortem analysis that indicated that the predominant slip systems were $\langle a \rangle$ Burgers vectors on basal planes, that is also the slip system reported to have the lowest CRSS in magnesium¹⁹. Bowed dislocations also tend to elongate along the Burgers vector to increase the screw component to minimize its energy, resulting in an elliptical shape such as the bowed segment (marked as 2) in Fig. 1d.

Dislocation Glide along Interfaces. Figure 1 shows the behavior of a single dislocation interacting with an extended β_1 precipitate. The glide dislocation is observed to be pinned and then eventually bypass the precipitates. The selected area is tilted to be near to the basal plane. The studied dislocation segment is marked with an

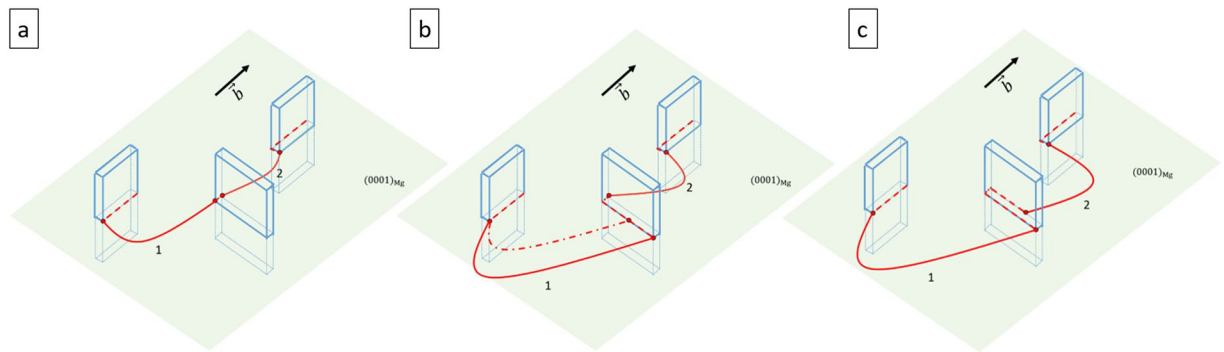


Figure 2. Schematics of precipitate-dislocation interactions depicting progression of the experimental images shown in Fig. 1. β_1 precipitates are oriented perpendicular to the basal plane depicted as plates with broad facets. Dislocations are constrained in the basal plane and the interfacial dislocations are represented by red dashed lines.

arrow in Fig. 1(a). With increasing stress during the indentation process, the initial dislocation starts to glide and reaches a new pinned configuration in Fig. 1b.

The pinned dislocation segment in Fig. 1(b) has been divided into part 1 and 2. It is noticeable that part 1 starts to glide (from Fig. 1b to c) by moving the right end on the precipitate facet. Figure 2 shows the corresponding schematic view of the observed dislocation-precipitate interaction. In Fig. 2a to b, the pinned segments 1 and 2 continue bowing as stress increases to a point when the right end of segment 1 moves along the precipitate interface. The dashed dotted line in Fig. 2(b) portrays an intermediate position of segment 1 between 9.05 s to 9.09 s in the *in situ* experiment. In this study, we define the dislocation configuration at the onset of interfacial glide as the critical condition. In order to maintain the continuity of the dislocation, the glide along the interface is expected to create additional dislocation line lengths at the interface, which are represented as red dash lines in Fig. 2. From Fig. 1b to c, once the interface glide initiates, the right end of segment 1 transitions to the departure side of precipitate in one frame (0.04 s). The mobility of the free end to glide along the precipitate interface is significantly higher than the bowing process leading to a fast transition from one pinned configuration to another one. In considering Figs 1 and 2, it should be noted that interfacial glide does not occur simultaneously for segments 1 and 2. Although the pinned segments 1 and 2 are formed from one single original dislocation, the bowing and interfacial glide behavior are independent from each other. This indicates that the pinned dislocation behavior depends on the segment between two pinned points rather than the whole dislocation, which is one of the basic assumptions in the following model.

Orientation-dependent effect. In Fig. 3, a foil region is examined that is oriented near to $(\bar{1}2\bar{1}3)$. Thus the foil plane lies 30° from the basal axis so that the precipitates are observed in a slant view. In section 2.a, dislocations initially interact with the narrow edge of the β_1 precipitate, followed by the formation of interfacial dislocations on the broad facets as interfacial glide occurs. In this *in situ* video, these interactions happen with the broad facets and display the different dislocation behaviors. Figure 3 shows two different precipitate-dislocation configurations at the same time. Two pinned dislocations are studied in this case: 1) A dislocation (marked as 1) is observed to glide in from the left bottom of the image and makes contact with the broad facet of the precipitates. 2) A dislocation (marked as 2) is observed to be pinned at the narrow edge of the precipitate near the left top of the image. In general, the two segments do not have to be in the same basal slip plane but in the schematic, are shown in the same plane for convenience. In Fig. 3(a), a purple dotted line is used as a reference to connect the two pinned nodes for Segment 2 and mark the orientation of the initial dislocation line. The main difference between the two pinned segments is the angle between the initial dislocation line direction and the broad precipitate facet. We define this angle as orientation angle. For segment 2, its initial dislocation line is about 30° away to the precipitate long axis, whereas the initial dislocation line of segment 1 is nearly parallel to it.

Segment 2 in Fig. 3 behaves similar to the dislocation in Fig. 1 in that it bows against the narrow edge and initiates interfacial glide when it reaches the critical condition. As in Fig. 3(c), after interfacial glide occurs at precipitates interfaces, segment 2 is pinned at the departure side. Without strong bowing, segment 2 is able to glide out of view at Fig. 3(d), which indicates a weak detachment force. In contrast, the behavior of segment 1 is completely different. As shown in Fig. 3(a), the segment 1 first approaches the broad interface of the precipitate and creates an interfacial dislocation marked as red dashed line in the schematics. Then, it gets pinned as depicted in Fig. 3(b). When it continues to glide, it bows around two pinned nodes in Fig. 3(c) and creates interfacial dislocations at precipitate interfaces as the dotted lines represent in Fig. 3(d). Comparing these two segments, from Fig. 3(a) to (c), both segments are bowed from the pinned nodes but segment 2 is able to glide at precipitate interface, whereas no interfacial glide occurs on segment 1 after it is pinned at the position depicted in Fig. 3(d).

The *in situ* experiment shows two different bowing configurations for segment 1 and 2. Segment 1 bows much more than segment 2. Because the back stress exerted from dislocations are related to the bowing shape, the difference in bowing shape is deemed to indicate these segments have different pinning stresses. The interfacial glide of segment 2 facilitates its propagation without the need to further increase bowing under the applied stress. There is no fundamental difference between segment 1 and 2 in terms of dislocation characteristics. As mentioned

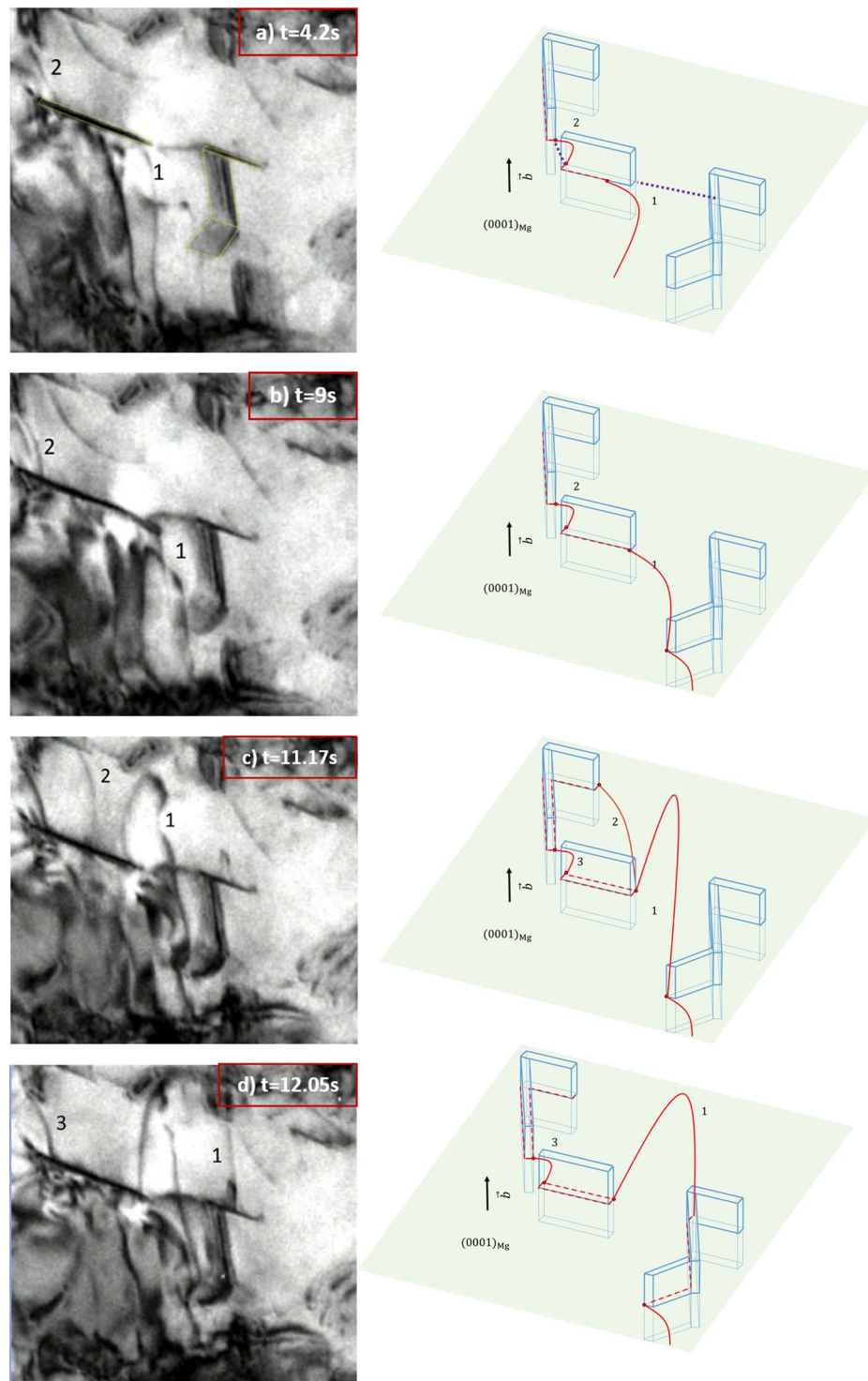


Figure 3. TEM images of motion of dislocations on basal (0001) plane thread through two parallel precipitates. Schematics in the right column correspond to the recorded frame at left. The viewing direction $[\bar{1}2\bar{1}3]$ of images relative to schematics is shown in schematic (a). The precipitates of interest are also outlined in (a). Initial dislocation line direction is represented as purple dotted line in (a). After segment 2 glides out of view, a following dislocation segment 3 is pinned in (c) and (d).

above, it is the precipitate-dislocation configurations that are different and the occurrence of the proposed interfacial glide mechanism reduces the pinning effect for specific dislocation-precipitate geometries. In this video, precipitates with lower orientation angles appear to exhibit a stronger pinning effect than those with larger angles.

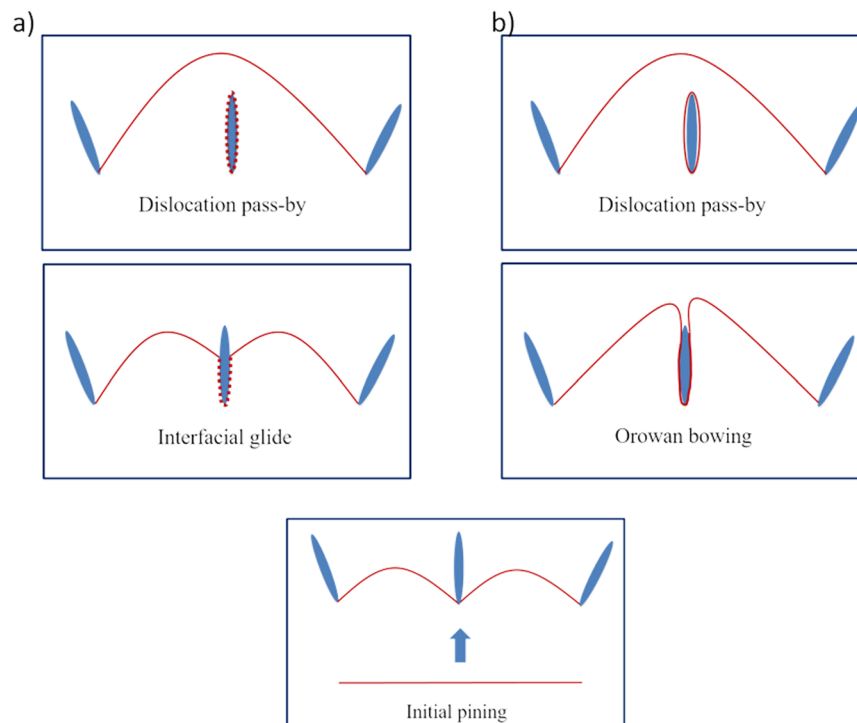


Figure 4. Schematic diagram of (a) proposed interfacial glide mechanism and (b) classical bowing mechanism for overcoming the given precipitate configuration. The dotted line around the center precipitate is the interfacial dislocation created by forward dislocations. Solid lines represent the initial position, critical condition, intermediate position and final position from bottom to top.

In summary, the different bowing configurations between these two segments gives an indication that the strengthening effect for single precipitate-dislocation interaction depends on the relative precipitate-dislocation orientation.

Discussion

In the *in situ* straining experiment, we have observed interfacial glide at broad facet of linear extended β_1 precipitates. Unlike the classical bowing mechanism in which the dislocation encircles the precipitate completely to form a loop, interfacial glide can create dislocations at interfaces without extensive bowing. For a given precipitate-dislocation configuration, Fig. 4 shows the difference between the two mechanisms. In both situations, dislocations are pinned at the leading edge of precipitates. However, after reaching the critical condition, interfacial glide is initiated in Fig. 4(a) showing a different sequence that occurs creating interfacial dislocations compared with the classical bowing shown in Fig. 4(b). The conditions that favor the unit process shown in 4 a) over 4 b) are analyzed below based on classical dislocation theory.

Dislocation Theory analysis. In order to comprehend this phenomenon, a model based on dislocation line tension is developed, as shown schematically as in Fig. 5.

In this model, we assume that given the different θ values for the two pinning points, the initiation of glide along the interface may be favored for one point over the other. It has to be mentioned that this is a generic scenario where dislocation get pinned by two extended precipitates. We do not presume any particular orientation between precipitates in the model although a 60° or 120° angle will occur between different β_1 precipitate variants. The conclusions are applicable for any general configuration of precipitates.

Once the dislocation begins to glide along the interface, it will lose the force equilibrium until it reaches another pinned position, normally the departure side of the precipitate. The detachment process is complicated and is not within the scope of this paper.

For the sake of mathematical simplicity, the bowed segment is treated as an arc with a radius of R . Angle α is the half of central angle for the bowed segment. For a given inter-particle spacing λ , a larger value of α shows a stronger bowing segment. We define $x = \sin(\alpha^*) = \frac{\lambda}{2R}$ as the bowing magnitude, ranging from 0 to 1, which is related to the strength of the pinning point, where α^* represents a critical value of α .

Figure 6 shows two possible configurations of the pinned dislocation, Fig. 6(a) for the case of no glide along interface and Fig. 6(b) for the case of dislocation glide along an interface.

E_1 is the dislocation energy at the critical condition. If there is no interfacial glide, Fig. 6(a), the pinned dislocation will continue bowing to a new position with an energy of E_2 . The area swept by dislocation bowing is S_1 and is related to the plastic work done. On the other hand, if interfacial glide occurs, Fig. 6(b), after infinite short amount of time, an infinitely small interfacial dislocation segment is created with an energy of E_1 and the new

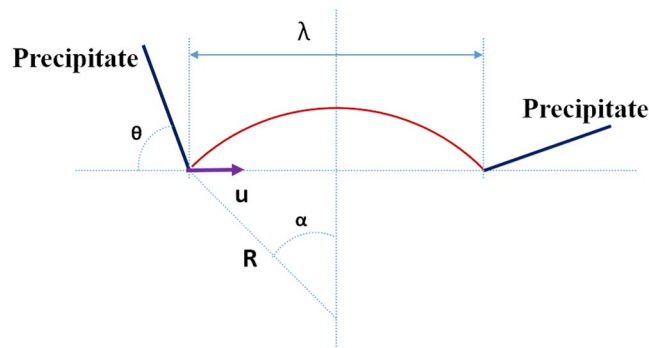


Figure 5. Dislocation-precipitate geometry for a pinned dislocation segment. The arrow indicates, as a reference, the initial unbowing dislocation line direction (\underline{u}). For the precipitate on the left, the orientation angle θ is defined as measured clockwise from \underline{u} to the trace of the broad facet of the precipitates. For the precipitate on the right, it is defined as measured counter clockwise.

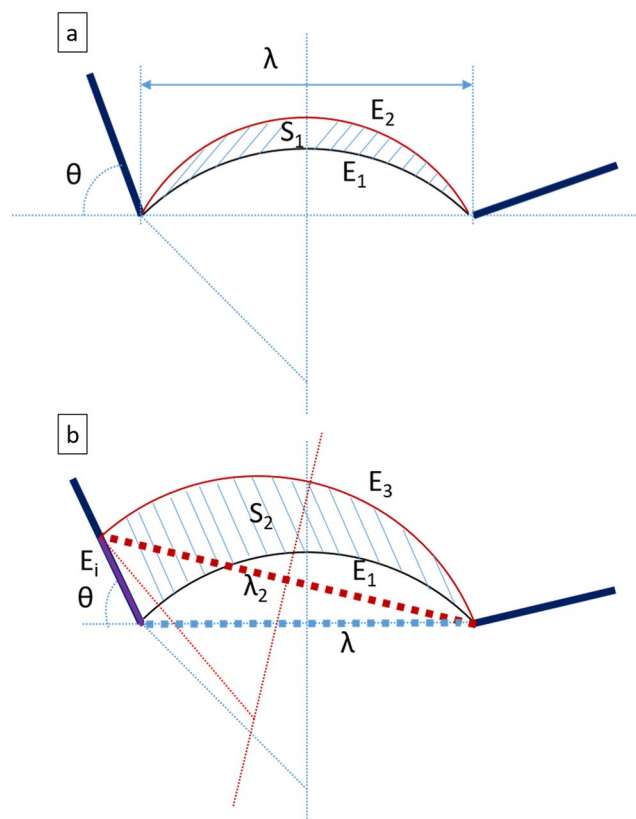


Figure 6. Schematic of two dislocation bowed shapes due to different energy configurations: (a) bowing without interfacial glide and (b) interfacial glide from the critical condition. The interfacial dislocation in (b) is represented by the purple line. This infinite small interfacial dislocation segment is exaggerated in the schematic for viewing purpose. The heavy dotted lines highlight the distance between pinned points.

curved dislocation has an energy of E_3 . The area swept by dislocation movement is S_2 . From an energy point of view, interfacial glide can initiate only if the energy of the second configuration, Fig. 6(b), is lower than the first one, Fig. 6(a). Therefore, the energetic criterion to initiate interfacial glide is as follows:

$$E_3 + E_i - \tau b S_2 < E_2 - \tau b S_1 \quad (2)$$

where τ is the Peach-Koehler stress. If the bowed dislocation is in force equilibrium at the critical condition, the external stress is equal to the back stress calculated from the dislocation.

$$\tau = \frac{T}{bR} = \frac{Gb}{2R} \quad (3)$$

where T is the line tension which is approximately $\frac{Gb^2}{2}$ using a constant line tension model.

Since the bowed shape is assumed to be an arc, i.e., it is insensitive to the direction of the Burgers vector, a constant line tension model is applied so that the dislocation line energy is only dependent on dislocation length. Then the energy of E_1 can be expressed as:

$$E_1 = \frac{Gb^2}{2} \left(2R \arcsin \frac{\lambda}{2R} \right) \quad (4)$$

After an incremental interfacial glide, as in Fig. 6(b), it is assumed that the new curved dislocation glides along the precipitate broad facet with no change in curvature, which gives its energy E_3 :

$$E_3 = \frac{Gb^2}{2} \left(2R \arcsin \frac{\lambda_2}{2R} \right) \quad (5)$$

It should be noticed that λ_2 is larger than λ so that the length of the new curved dislocation is longer than the dislocation when it is in the critical condition. This leads to an increase in the energy δE . The energy criteria can be revised as:

$$\delta E + E_i + \tau b(S_1 - S_2) < E_2 - E_1 \quad (6)$$

The evolution from E_1 to E_2 is because of a change in the radius of curvature. Since the change is infinitesimal, the criterion becomes:

$$\delta E + E_i + \tau b(S_1 - S_2) < dE \quad (7)$$

The right side of equation (7) is a derivative of equation (4) with regard to radius R . Its expression is given as:

$$dE = \frac{Gb^2}{2} \left(\frac{2 \frac{\lambda}{2R}}{\sqrt{1 - \left(\frac{\lambda}{2R}\right)^2}} - 2 \arcsin \frac{\lambda}{2R} \right) dR \quad (8)$$

To solve δE ,

$$\begin{aligned} \delta E &= E_3 - E_1 \\ \delta E &= \frac{Gb^2}{2} * 2R \left(\arcsin \frac{\lambda_2}{2R} - \arcsin \frac{\lambda}{2R} \right) \end{aligned} \quad (9)$$

Because the difference between λ_2 and λ is infinitesimally small, the value of the expression in parentheses in equation (9) can be solved by Taylor expansion. Expanding $\arcsin x$ on $x = \frac{\lambda}{2R}$ yields

$$\arcsin x = \arcsin \left(\frac{\lambda}{2R} \right) + \frac{1}{\sqrt{1 - \left(\frac{\lambda}{2R}\right)^2}} \left(x - \frac{\lambda}{2R} \right) + o \left(x - \frac{\lambda}{2R} \right)^2 \quad (10)$$

The last term of this polynomial is a higher order term that can be ignored in the following derivation. Utilizing the approximation in equation (10) and setting $x = \arcsin \frac{\lambda_2}{2R}$, the equation (9) can be approximately written as

$$\delta E = E_3 - E_1 = \frac{Gb^2}{2} \frac{1}{\sqrt{1 - \left(\frac{\lambda}{2R}\right)^2}} (\lambda_2 - \lambda) \quad (11)$$

λ_2 can be expressed as

$$\begin{aligned} \lambda_2 &= \sqrt{(\lambda + dl \cos \theta)^2 + (dl \sin \theta)^2} \\ \lambda_2 &= \sqrt{\lambda^2 + 2\lambda dl \cos \theta + dl^2} \end{aligned} \quad (12)$$

where dl is the length of the interfacial dislocation, which is also an infinitesimally small value. Hence, $\lambda_2 - \lambda$ is infinitesimally small. The approximation of that difference is in the same manner as the previous Taylor expansion. The result can be expressed as

$$\lambda_2 - \lambda = \frac{1}{2\lambda} (2\lambda dl \cos \theta + dl^2) \quad (13)$$

Ignoring the higher order term dl^2 , the final expression for δE is

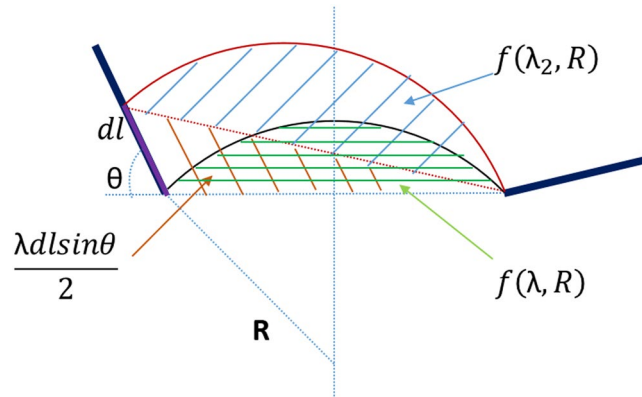


Figure 7. Schematic shows area of different regions. The green shaded area is the dislocation swept area before interfacial glide is initiated. The sum of orange and blue shaded area is the swept area caused by bowing and interfacial glide.

$$\delta E = E_3 - E_1 = \frac{Gb^2}{2} \frac{1}{\sqrt{1 - \left(\frac{\lambda}{2R}\right)^2}} dl \cos \theta \tag{14}$$

To solve S_1 and S_2 , we come up with a function defining the green shaded area in Fig. 7. The function can be expressed as

$$S = f(\lambda, R) = R^2 \arcsin\left(\frac{\lambda}{2R}\right) - \frac{\lambda}{2} \sqrt{R^2 - \left(\frac{\lambda}{2}\right)^2} \tag{15}$$

The expression for S_1 is basically the derivative of $f(\lambda, R)$ with respect to radius R .

$$S_1 = \frac{\partial f}{\partial R}(-dR) = \left[-\frac{2\lambda R}{\sqrt{4R^2 - \lambda^2}} + 2R \arcsin\left(\frac{\lambda}{2R}\right) \right](-dR) \tag{16}$$

Mathematically dR is defined as the difference between radii of E_2 and E_1 , which is negative for this bowing configuration. Hence, the negative sign for dR is to ensure a positive value of dR .

It takes more effort to acquire S_2 since it involves three shaded areas in Fig. 7. S_2 can be calculated as the sum of blue and orange shaded area after subtracting the area marked in green.

$$S_2 = f(\lambda_2, R) + \frac{\lambda dl \sin \theta}{2} - f(\lambda, R) \tag{17}$$

A similar approximation method is used to solve $f(\lambda_2, R) - f(\lambda, R)$. The result is given as

$$S_2 = \left[\frac{R}{\sqrt{4 - \frac{\lambda^2}{R^2}}} - \frac{2R^2 - \lambda^2}{2\lambda\sqrt{4R^2 - \lambda^2}} \right] dl \cos \theta + \frac{\lambda dl \sin \theta}{2} \tag{18}$$

Up to this point, most of the terms in the energy criteria equation (20) are solved except for the interfacial dislocation energy, E_i . Results from earlier studies suggest that the energy of interfacial dislocations is lower than that in the matrix²⁰. The line energy at the particle interface is given as:

$$E_i = \frac{Gb^2}{2} K dl \tag{19}$$

where K is the relaxation parameter which is related to the interface property such as coherency and atomic bonding strength. The presence of interfacial dislocations is believed to alter the interface atomic structure locally due to dislocation core relaxation and spreading that lowers the energy of the interfacial dislocation. The value of K ranges from 0 (interfacial dislocations have no energy) to 1 (no interfacial dislocation relaxation). We will use this equation to study how interfaces affect interfacial glide.

Inserting all the energy terms into the energy criteria (7) and simplifying, results in the following equation:

$$K - \sin \theta x + \sqrt{1 - x^2} \cos \theta < 0 \tag{20}$$

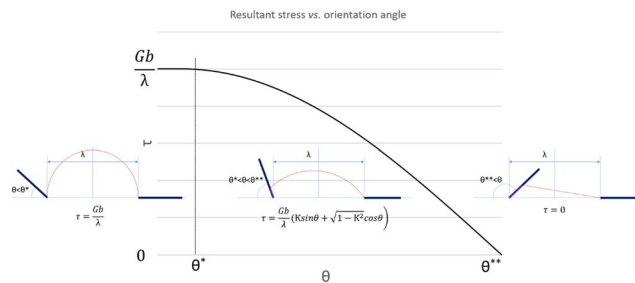


Figure 8. The resultant stress τ is monotonically decreasing because of interfacial glide. As the schematics shows no interfacial glide occurs when orientation angle θ is smaller than θ^* . The stress is a function of θ when orientation angle is between θ^* and θ^{**} . The interfacial glide will occur spontaneously when θ is larger than θ^{**} .

It should be noted that equation (20) is valid for θ from 0 to 180° even though the schematic in Figs 6 and 7 only shows θ smaller than 90°.

Model application. For any given precipitate-dislocation configuration, equation (20) can be used to predict whether or not interfacial glide is energetically favorable. For example, if the pinning precipitates are perpendicular to initial dislocation line direction, then θ is set equal to 90°. For this geometry, equation (20) yields the energy criteria that are required to satisfy $K < x$. If interfacial glide can occur, equation (20) must solve a value of x within the range from 0 to 1. In the situation above, if no interfacial dislocation relaxation exists in this interface ($K = 1$), there is no resolved x from equation (20) meaning no interfacial glide is allowed. In fact, for $K = 1$, for any given value of θ we input into equation (20), there is no solution for x . In conclusion, the energy criteria suggest that the root cause of interfacial glide is the existence of interfacial dislocation relaxation.

For any $K < 1$, interfacial glide may be activated but not necessarily for all precipitate-dislocation configurations. Solving the equation (20) under different constraints provides the conditions under which interfacial glide can occur. The mathematical derivation is omitted.

1. When $K < 1$, interfacial glide is not allowed if orientation θ is smaller than θ^* where

$$\theta^* = \arccos\sqrt{1 - K^2} \quad (21)$$

2. When $K < 1$ and $\theta^* < \theta$, interfacial glide happens when

$$x = K\sin\theta + \sqrt{1 - K^2}\cos\theta \quad (22)$$

3. When $K < 1$ and $\theta > 90^\circ$, the left side of equation (20) is always smaller than zero if θ is larger than θ^{**}

$$\theta^{**} = \pi - \arccos K \quad (23)$$

When θ is larger than θ^{**} , interfacial glide will occur spontaneously.

Case 1 indicates a threshold value for initiation of interfacial glide. It also implies an orientation-dependent effect. If the precipitate has orientation factor θ smaller than θ^* , no interfacial glide is allowed meaning the bowing magnitude of the pinned dislocation, $\frac{\lambda}{2R}$, can reach a value of 1. Recall that equation (3) can be written in terms of the bowing magnitude x to reflect the maximum back stress when dislocation reaches the critical condition.

$$\begin{aligned} \tau &= \frac{Gb}{2R} = \frac{Gb}{\lambda}x \\ \tau &= \frac{Gb}{\lambda}(K\sin\theta + \sqrt{1 - K^2}\cos\theta) \end{aligned} \quad (24)$$

From Case 2, the resultant stress calculated for the critical condition is a function of the orientation factor θ . It follows that the stress τ is monotonically decreasing with θ when it ranges from θ^* to θ^{**} . The function of equation (24) is plotted in Fig. 8. This explains the experimental result in section 2.b where dislocations are bowed strongly for segment 1 and no interfacial glide is allowed to initiate whereas for segment 2, it is easy for interfacial glide to occur. Because of the different precipitate-dislocation configurations for the two segments, the one with smaller precipitate orientation angle is more difficult or even impossible to initiate interfacial glide and this is the case for segment 1. Although it is not possible to measure the external stress from the *in situ* video, the shape of bowed dislocation can be used to infer the level of stress acting on dislocation. The stronger bowing shape of segment 1 indicates a higher back stress against the external stress, which supports the hypothesis that interfacial glide is sensitive to precipitate orientation and may have an influence on the overall precipitation hardening. In addition, Case 3 provides an interesting situation in which the dislocation segment will spontaneously glide along the interface because the energy criteria is automatically satisfied when θ is larger than θ^{**} . This may explain the result in section 2.b where the initial incoming dislocation segment 1 directly deposits interfacial dislocations on

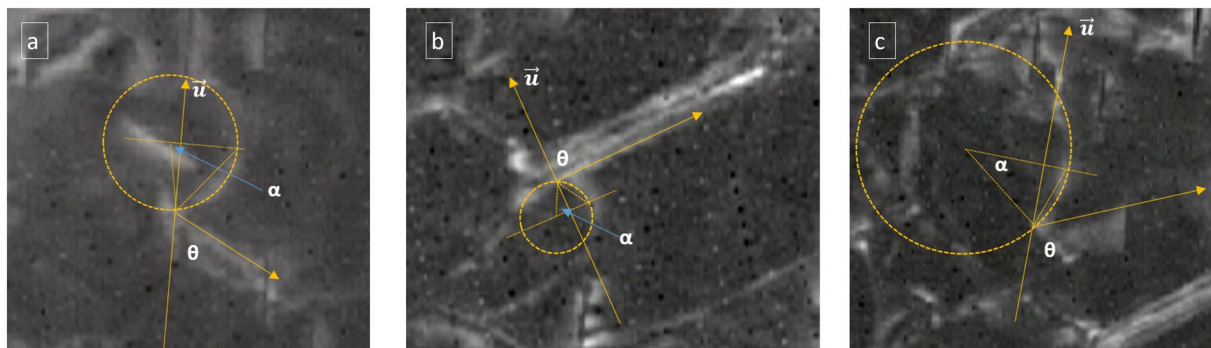


Figure 9. Method for measuring the half central angle for three critical conditions used to determine the relaxation parameter K . All images are extracted from *in situ* video recorded in dark field condition with near basal orientations. The yellow arrows show broad facet orientations and the initial dislocation line direction.

	$\theta/^\circ$	$\alpha^*/^\circ$	x	K
a)	62	81.9	0.99	0.81
b)	90	64.2	0.90	0.90
c)	113	36.1	0.59	0.86

Table 1. Relaxation parameter determination on three different configurations.

the first precipitate interfaces. However, this mechanism is only accountable for pinning at the leading edge of the precipitate. After the interfacial glide, the dislocations become anchored at the departure end of the precipitate and thus the strengthening also depends on the detachment process. The pinning effect from the departure side is unsolved. For example, dislocation segment 1 in Fig. 1 receive strong pinning from the left end resulting in a strong bowing shape whereas segment 2 in Fig. 3 easily glides out of view from departure side without severe bowing. The overall precipitation strengthening is determined by the higher pinning effect from leading and departure end. The detachment process is currently under investigation.

As indicated, the interface relaxation parameter K is of great significance in determining if interfacial glide is to be expected. Equation (20) provides a method for determining the interface relaxation parameter K . The value of K can be determined if the orientation angle θ is measured from *in situ* experiments and the bowing magnitude is extracted from critical conditions. However, practically, the bowing magnitude is difficult to precisely measure due to the image quality and strain field around dislocations and precipitates. A shape fitting method was used to increase the measurement accuracy. A circle is matched to the curved segment, hence the half central angle α is measured graphically from the critical condition and the bowing magnitude is determined. In Fig. 9, three critical conditions are extracted from *in situ* videos. The first one comes from section 2.a and the other two come from another video but all in the same basal view direction. The results are summarized in Table 1. Although the three critical conditions have different precipitate-dislocation configurations, the calculated relaxation parameters are relatively consistent. The average value of K is 0.86. The relative constant value of K suggests that the interface dislocation relaxation is closely related to interface itself, which is thought to be linked to the interface geometry and atomic structure²⁰. Research characterizing this relaxation parameter in other alloy systems^{20,21}, especially in oxide dispersion strengthened (ODS) alloys suggests that interface dislocation relaxation affects the creep behavior of those alloys. In the ODS systems, the reinforcing particles are incoherent with the matrix. A lower bound for relaxation parameter has been determined to be 0.66 for the superalloy INCONEL MA754²⁰. An upper bound value for K of 0.93 has been determined for MA6000²¹. Although this phenomenon is widely observed, the physical meaning remains unclear. In semi-coherent metallic interfaces²², dislocation core spreading may lead to interface relaxation. Incoherent or semi-coherent interfaces which have relatively lower shear strength of the interface can ease atomic rearrangement and facilitate local interface diffusion resulting in a lower interface dislocation energy²³. The value of K of 0.85 in the present work seems to fall into a reasonable range. Although β_1 precipitates in Mg are generally reported to be coherent²⁴, the samples characterized in this study were over-aged and may have resulted in semi-coherent precipitates. The atomistic mechanism to lower the interfacial dislocation energy cannot be interpreted with the current model which is based on linear elasticity, and should be investigated by atomistic simulations.

The dislocation energy model in this study explains the theoretical foundation of interfacial glide and shows the orientation-dependent effect. Nevertheless, it should be recognized that many simplifications have been made in deriving this model. In reality, dislocation energy is sensitive to Burgers vector and surrounding strain field from other dislocations and precipitates. Calculations related to individual precipitate-dislocation interaction are only suitable for ideal situations. A more accurate study may involve use of dislocation dynamics (DD) simulations. A better understanding of interfacial glide is believed to be important for alloy development. It could be a

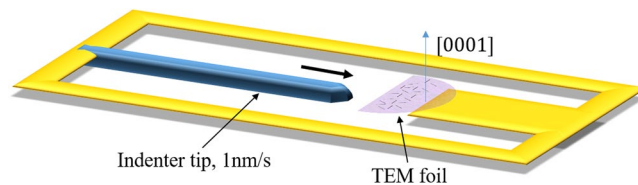


Figure 10. Schematic of *in situ* straining setup. The TEM foil in this figure is selected with its normal (blue arrow) closely parallel to [0001]. Black dashes in foil represent precipitates of three different variants. The indentation direction is indicated by thick black arrow.

general mechanism for dislocations interactions with linear extended precipitates. From the analysis of the relaxation parameter K , this study suggests that interface engineering may play an important role in determining the strengthening effect due to extended precipitates.

Conclusions

In situ straining in TEM is performed on over-aged Mg-2.35% wt.% Nd binary alloy. The unit process for precipitate-dislocation interaction was observed for extended lath β_1 precipitates. A dislocation based model is developed to analyze the unit process. The key findings from the experimental characterization and theoretical analysis are summarized below.

1. The pinned dislocation may glide along the precipitate broad facet to overcome precipitate blocking, thereby creating interfacial dislocations.
2. An orientation-dependent effect is observed suggesting a stronger pinning effect for precipitates with low orientation angle θ , as defined in Fig. 5.
3. Dislocation theory-based analysis shows that the proposed interfacial glide mechanism is energetically favorable if interface dislocation relaxation exists.
4. The model shows that the resultant stress for glide is affected by interfacial glide which is determined by the orientation angle θ and an interface relaxation parameter K that ranges from 1 (no glide along the interface implying high resistance to creating interfacial dislocation segments) to 0 (easy glide along the interface, low interface resistance to creating interfacial dislocation segments).
5. A higher value of θ and a lower value of K will result in a lower value of the glide stress for single dislocation, and ultimately a reduced level of strengthening from leading edge of the precipitate.

Experimental Methods

An as-cast Mg-2.35 wt.% Nd binary alloy provided by CanmetMATERIALS was used in this investigation. The alloy was prepared by resistance heating in a steel crucible under a protective atmosphere of CO_2 and 0.5% SF_6 gas and then poured into a mold with diameter of 3.5 inches. Castings were solution treated at 530 °C for 3 hours and water quenched. The aging condition was 9 hours at 250 °C to ensure that β_1 was the dominant precipitate. Specimens for transmission electron microscopy (TEM) were mechanically thinned to 100 μm and electropolished following the procedure from Nie and Muddle²⁵. The edge of specimen is preferentially electropolished to electron transparency. The electropolished sample was glued to the stage of a Hysitron PI95 TEM Picoindenter leaving the transparent region facing the 1 μm flat punch indenter tip. Figure 10 schematically shows the *in situ* straining setup. Local deformation is introduced by indentation at a displacement rate of 1 nm/s and dislocation activity was recorded by a CCD camera at a frame rate of 25 frames/second. Since the area of the TEM foil deformed by the indenter tip is small with respect to the grain size, the deformed region can be regarded as a part of a single crystal. Most of selected foils have an orientation near basal plane and some near to $(\bar{1}\bar{2}\bar{1}3)$ plane. Experiments are conducted in a JEOL 2010F transmission electron microscope.

Data Availability. All data generated or analyzed during this study are included in this published article (and its Supplementary Information files).

References

1. Miller, W. *et al.* Recent development in aluminium alloys for the automotive industry. *Materials Science and Engineering: A* **280**, 37–49 (2000).
2. Kulekci, M. K. Magnesium and its alloys applications in automotive industry. *The International Journal of Advanced Manufacturing Technology* **39**, 851–865 (2008).
3. Heinz, A. *et al.* Recent development in aluminium alloys for aerospace applications. *Materials Science and Engineering: A* **280**, 102–107 (2000).
4. Nie, J.-F. Precipitation and hardening in magnesium alloys. *Metallurgical and Materials Transactions A* **43**, 3891–3939 (2012).
5. Nie, J. Effects of precipitate shape and orientation on dispersion strengthening in magnesium alloys. *Scripta Materialia* **48**, 1009–1015 (2003).
6. Antion, C. *et al.* Hardening precipitation in a Mg–4Y–3RE alloy. *Acta Materialia* **51**, 5335–5348 (2003).
7. Apps, P., Karimzadeh, H., King, J. & Lorimer, G. Precipitation reactions in magnesium-rare earth alloys containing yttrium, gadolinium or dysprosium. *Scripta Materialia* **48**, 1023–1028 (2003).

8. Gao, X. *et al.* Microstructure evolution in a Mg–15Gd–0.5 Zr (wt.%) alloy during isothermal aging at 250 C. *Materials Science and Engineering: A* **431**, 322–327 (2006).
9. Kainer, K. U. & Wiley Online Library (Online service). (Wiley-VCH [Imprint] John Wiley & Sons, Hoboken, 2006).
10. Liu, H., Wang, Y. & Nie, J.-F. in *Proceedings of the 3rd World Congress on Integrated Computational Materials Engineering (ICME 2015)*. 63–71 (Springer).
11. Kelly, A. & Nicholson, R. *Strengthening methods in crystals*. (Halsted Press Division, 1971).
12. Ardell, A. Precipitation hardening. *Metallurgical Transactions A* **16**, 2131–2165 (1985).
13. Nembach, E. Particle strengthening in metals and alloys John Wiley & Sons, New York (1997).
14. Reppich, B., Cahn, R., Haasen, P. & Kramer, E. *Material Science and Technology: A Comprehensive Treatment*. Vol. 6 (VHC, Weinheim, 1993).
15. Zhu, A. & Starke, E. Strengthening effect of unsharable particles of finite size: a computer experimental study. *Acta materialia* **47**, 3263–3269 (1999).
16. Queyreau, S., Monnet, G. & Devincere, B. Orowan strengthening and forest hardening superposition examined by dislocation dynamics simulations. *Acta Materialia* **58**, 5586–5595 (2010).
17. Liu, H., Gao, Y., Qi, L., Wang, Y. & Nie, J.-F. Phase-Field Simulation of Orowan Strengthening by Coherent Precipitate Plates in an Aluminum Alloy. *Metallurgical and Materials Transactions A* **46**, 3287–3301 (2015).
18. Bulatov, V. & Cai, W. *Computer simulations of dislocations*. Vol. 3 (Oxford University Press on Demand, 2006).
19. Britton, T., Dunne, F. & Wilkinson, A. in *Proc. R. Soc. A*. 20140881 (The Royal Society).
20. Arzt, E. & Wilkinson, D. Threshold stresses for dislocation climb over hard particles: the effect of an attractive interaction. *Acta Metallurgica* **34**, 1893–1898 (1986).
21. Häussler, D., Bartsch, M., Messerschmidt, U. & Reppich, B. HVTEM in situ observations of dislocation motion in the oxide dispersion strengthened superalloy MA 754. *Acta materialia* **49**, 3647–3657 (2001).
22. Gao, H., Zhang, L. & Baker, S. P. Dislocation core spreading at interfaces between metal films and amorphous substrates. *Journal of the Mechanics and Physics of Solids* **50**, 2169–2202 (2002).
23. Wang, J., Hoagland, R., Liu, X. & Misra, A. The influence of interface shear strength on the glide dislocation–interface interactions. *Acta Materialia* **59**, 3164–3173 (2011).
24. Xu, Z., Weyland, M. & Nie, J. On the strain accommodation of β 1 precipitates in magnesium alloy WE54. *Acta Materialia* **75**, 122–133 (2014).
25. Nie, J. & Muddle, B. Characterisation of strengthening precipitate phases in a Mg–Y–Nd alloy. *Acta Materialia* **48**, 1691–1703 (2000).

Acknowledgements

This work was supported by the U.S. Department of Energy, Office of Basic Energy Sciences, Division of Materials Sciences and Engineering under Award #DE-SC0008637 as part of the Center for Predictive Integrated Structural Materials Science (PRISMS Center) at University of Michigan. We gratefully acknowledge Dr. Bruce Williams of CanmetMATERIALS who provided the Mg–Nd alloy used in this study. Electron Microscopy was conducted at the Michigan Center for Materials Characterization at University of Michigan.

Author Contributions

A.M. and J.E.A. designed the topic of the study. Z.H. perform the *in situ* straining experiment and dislocation-theory based analysis. Z.H. prepared the first version of manuscript and all authors participated in the discussion and revision of the manuscript.

Additional Information

Supplementary information accompanies this paper at <https://doi.org/10.1038/s41598-018-20629-1>.

Competing Interests: The authors declare that they have no competing interests.

Publisher's note: Springer Nature remains neutral with regard to jurisdictional claims in published maps and institutional affiliations.



Open Access This article is licensed under a Creative Commons Attribution 4.0 International License, which permits use, sharing, adaptation, distribution and reproduction in any medium or format, as long as you give appropriate credit to the original author(s) and the source, provide a link to the Creative Commons license, and indicate if changes were made. The images or other third party material in this article are included in the article's Creative Commons license, unless indicated otherwise in a credit line to the material. If material is not included in the article's Creative Commons license and your intended use is not permitted by statutory regulation or exceeds the permitted use, you will need to obtain permission directly from the copyright holder. To view a copy of this license, visit <http://creativecommons.org/licenses/by/4.0/>.

© The Author(s) 2018